HAL
open science

Three-dimensional analysis of precursors to non-viscous dissipation in an experimental turbulent flow

P. Debue, V. Valori, C. Cuvier, F. Daviaud, J.-M. Foucaut, Jean-Philippe Laval, C. Wiertel, V. Padilla, B. Dubrulle

To cite this version:

P. Debue, V. Valori, C. Cuvier, F. Daviaud, J.-M. Foucaut, et al.. Three-dimensional analysis of precursors to non-viscous dissipation in an experimental turbulent flow. Journal of Fluid Mechanics, 2021, 914, pp.A9. 10.1017/jfm.2020.574 . hal-03297759

HAL Id: hal-03297759

https://hal.science/hal-03297759

Submitted on 6 Oct 2022

HAL is a multi-disciplinary open access archive for the deposit and dissemination of scientific research documents, whether they are published or not. The documents may come from teaching and research institutions in France or abroad, or from public or private research centers.

L'archive ouverte pluridisciplinaire **HAL**, est destinée au dépôt et à la diffusion de documents scientifiques de niveau recherche, publiés ou non, émanant des établissements d'enseignement et de recherche français ou étrangers, des laboratoires publics ou privés.

3D analysis of precursors to non-viscous dissipation in an experimental turbulent flow

P. Debue [1], V. Valori [1], Ch. Cuvier[2] , F. Daviaud [1], J-M. Foucaut[2], J-P. Laval[2] , C. Wiertel[1] V. Padilla[1] and B. Dubrulle[1]†

[1] Université Paris-Saclay, CEA, CNRS, SPEC, CEA Saclay, F-91191 Gif-sur-Yvette, France.

[2]Univ. Lille, CNRS, ONERA, Arts et Metiers Institute of Technology, Centrale Lille, UMR 9014-LMFL-Laboratoire de Mécanique des Fluides de Lille - Kampé de Fériet, F-59000, Lille, France

(Received xx; revised xx; accepted xx)

We study the 3D structure of turbulent velocity fields around extreme events of local energy transfer in the dissipative range. Velocity fields are measured by Tomographic Particle Velocimetry at the center of a von Kármán flow with resolution reaching the Kolmogorov scale. The characterization is performed through both direct observation and an analysis of the velocity gradient tensor invariants at the extremes. The conditional average of local energy transfer on the second and third invariants seems to be the largest in the sheet zone, but the most extreme events of local energy transfer mostly correspond to the vortex stretching topology. The direct observation of the velocity fields allows for identification of three different structures : the screw- and roll- vortices, and the U-turn. They may correspond to a single structure seen at different times or in different frames of reference. The extreme events of local energy transfer come along with large velocity and vorticity norms, and the structure of the vorticity field around these events agrees with previous observations of numerical works at similar Reynolds numbers.

1. Introduction

In 1949, Onsager conjectured that for rough enough velocity fields, energy dissipation could arise without the help of viscosity (**??**). This conjecture was proven by **?**, who used convex integration methods introduced by De Lellis and Szekelyhidi (**???**) and the concept of Mikado flow (**?**) to prove the existence of weak solutions of Euler equations, that do not conserve energy. Reversely, Onsager also conjectured that non-viscous dissipation would not happen for velocity fields that are h-Holder continuous with $h > 1/3$. This conjecture was first proven by **?** , while a simple and elegant proof was later provided by **?**, using the energy balance equation for weak solutions of the 3D incompressible Navier-Stokes equations (INSE) :

$$\partial_t \frac{u_i^2}{2} + \partial_j[u_j(\frac{u_i^2}{2} + p)] = \nu \Delta \frac{u_i^2}{2} - \nu \partial_j u_i \partial_j u_i + D(\mathbf{u}) \tag{1.1}$$

In this equation, $\mathbf{u}$ is a weak solution of the 3D INSE, and the derivatives should therefore be understood in the sense of distributions. This energy balance is very similar to that of ordinary 3D INSE, except for an additional energy dissipation term $D(\mathbf{u})$ stemming from the lack of regularity of the velocity field. $D(\mathbf{u})$ is defined as follows :

$$D(\mathbf{u}) = \lim_{\ell \to 0} \Pi_{DR}^{\ell} \tag{1.2}$$

† Email address for correspondence: berengere.dubrulle@cea.fr

where Π^{ℓ}_{DR} originates from the non-linear (inertial) terms of the 3D INSE :

$$\Pi^{\ell}_{DR}(\mathbf{x}) = \frac{1}{4}\int \boldsymbol{\nabla}\phi^{\ell}(\boldsymbol{\xi}) \cdot \boldsymbol{\delta}\mathbf{u}(\boldsymbol{\delta}\mathbf{u})^2 d^3\boldsymbol{\xi}$$

ϕ^{ℓ} is a smooth filtering function and $\boldsymbol{\delta}\mathbf{u}$ is the velocity increment, depending implicitly on $\mathbf{x}$ and $\boldsymbol{\xi}$: $\boldsymbol{\delta}\mathbf{u}(\mathbf{x},\boldsymbol{\xi}) = \mathbf{u}(\boldsymbol{x}+\boldsymbol{\xi}) - \mathbf{u}(\mathbf{x})$.

Duchon and Robert proposed to consider as physically relevant only those solutions for which $D(\mathbf{u}) \geqslant 0$, which they call "dissipative solutions", $D(\mathbf{u})$ being the "inertial dissipation". They showed that the weak solutions exhibited by **?** were dissipative solutions ; however, they did not exhibit any solution for which $D(\mathbf{u}) \neq 0$. A balance equation similar to 1.1 holds if $\nu = 0$, i.e. in the case of the 3D incompresssible Euler equations. Duchon and Robert also showed that a solution to the 3D incompressible Euler equations that is the strong limit of a sequence of dissipative weak solutions to the Navier-Stokes equations would be a dissipative solution ($D(\mathbf{u}) \geqslant 0$). They further proved that in the case where $\nu = 0$, $D(\mathbf{u}) = 0$ if the velocity field is h-Holder continuous with $h > 1/3$ (in particular if the velocity field is regular, i.e. if $h = 1$), thus proving Onsager's conjecture. If $h \leqslant 1/3$, $D(\mathbf{u})$ may well be non-zero : additional dissipation would then arise from the roughness of the velocity field. This can be understood from the definition of h-Holder continuity since then $|\boldsymbol{\delta}\mathbf{u}| = O(|\xi|^h)$ and $\Pi^{\ell}_{DR} = O(\ell^{3h-1})$. If $h \leqslant 1/3$, Π^{ℓ}_{DR} does not tend to 0 when ℓ tends to 0. On the other hand, if $h = 1$, then $D(\mathbf{u}) = 0$: therefore, if $D(\mathbf{u}) > 0$, the velocity field is necessarily singular.

What is then the relevance of the above considerations towards a real velocity field ? Real flows obey incompressible Navier-Stokes equations under at least two conditions : C1) the smallest scales are larger than the mean free path ; C2) the velocity is smaller than the speed of sound, resulting in $Ma = u/c_s \ll 1$. At the location of a mathematical singularity of the Navier-Stokes equations, the velocity field would extend over arbitrarily small scales, becoming infinite (arbitrarily large) as the scale decreases (**?**). Therefore, conditions C1 and C2 would not apply anymore and additional physics would come into play, presumably hindering the growth of any mathematical singularity. For instance, one can speculate that the growth of a singularity would generate compressible effects with the associated dissipation mechanism, replacing the inertial dissipation that might have taken place in the incompressible solution by shocks.

To understand the general nature of dissipation processes in incompressible fluids, it is therefore of interest to investigate in more detail what is happening in an experimental flow at places where Π^{ℓ}_{DR} is very large at very small scales (of the order of the Kolmogorov scale) : such places may be prints of inertial dissipation occurring in a mathematical solution to the 3D INSE, which would be replaced, in a real flow, by physical phenomena not included in those equations. Therefore, we study the topology of the velocity field around these events to try to understand how they form. Such a work was initiated in **?**, where extreme events of a 2D version of Π^{ℓ}_{DR} are studied in 2D-3C velocity fields measured by stereoscopic particle image velocimetry (SPIV) . Four kinds of structures had been observed, but it was not possible to know whether they were different structures or different cross-sections, possibly observed at different times, of a single one. The use of tomographic particle image velocimetry (TPIV) now allows us to perform 3D-3C measurements of the velocity field and therefore to analyze the full 3D structure of the detected events.

The article is organized as follows : the experimental set-up is detailed in 2. The statistics of the quantity underlying the detection criterion as well as the intensity of the detected events are reported in Sec. 3. The structure of the velocity field around the

detected events is then characterized with the velocity gradient tensor (VGT) invariants method in Sec. 4 and by direct observations in Sec. 5. The results are then discussed in Sec. 6 before a conclusion is drawn in Sec. 7.

2. Experimental set-up

The velocity fields are measured at the center of a von Kármán flow, as shown on Fig. 1(a). Such area corresponds to the location where the turbulence is the most homogeneous and isotropic, even though it is not rigorously perfectly homogeneous and isotropic (see e.g. **?**). Previous measurements of spectra, local energy transfer, dissipation or structure functions **??** in that area were found to be in agreement with results from direct numerical simulation of homogeneous isotropic turbulence, and exhibit universality **?**. Therefore, we expect the results described in the present paper to be fairly general.

This flow is generated by two counter-rotating impellers in a cylinder whose radius is $R = 10$ cm. The impellers have eight curvated 2 cm-high blades, their diameter is 9.25 cm and the distance between the blades is 14 cm. They rotate at the same frequency F, in the direction such that the concave side of the blades pushes the fluid. The resulting flow is characterized by a Reynolds number Re based on the impeller rotation frequency F, the cylinder radius R and the fluid viscosity ν :

$$Re = \frac{2\pi R^2 F}{\nu} \tag{2.1}$$

In this article, the fluid is water at 20°C, and $\nu = 10^{-6}$ m^2/s. The temperature of the fluid is kept constant by means of a cooling system and the impeller rotation frequency is monitored by SCAIME torquemeters ; it varies by less than 1%. For $Re > 6000$, the flow is fully turbulent (**?**). The average flow is then made of two counter-rotating cells ; at the center (i.e. at the intersection of the equatorial plane and of a meridian plane), there is a strong shear but the average velocity is very small. At large Reynolds numbers, the dimensionless root-mean-square (rms) of the velocity fluctuations is independent of the Reynolds number ; the rms of the fluctuations along x and z axis are about $V/3$ and the rms of the fluctuations along the z axis is about $V/5$, with $V = 2\pi RF$ the typical large scale velocity. The global average dissipation rate ϵ can be measured with the torquemeters ; its dimensionless value $\epsilon^* = \epsilon/(2\pi F)^3 R^2)$ is also independent of Re in the limit of large Reynolds numbers, it is equal to 4.8×10^{-2} in this limit.

The size of the velocity field is 5 cm$\times$3.5 cm$\times$0.67 cm. It is measured by TPIV. Five Imager sCMOS cameras are placed in the same equatorial plane and acquire pictures with different viewing angles, as shown on Fig. 1(b). They are equipped with Zeiss Milvus 2 lenses mounted on Lavision Scheimpflugs ; the numerical aperture is $f_\# = 11$ and the focal length is 100 mm. The diffraction spot is then 2.8 pixels wide and the depth of field is 7 mm. An outer tank with flat faces and filled with water allows for the reduction of optical distortions due to the interface between air and water. The particles are glass hollowspheres of 10 μm diameter ; they are lighted by a Solo II PIV laser. A mirror is used so that the laser beam crosses the measurement volume twice ; thus, all cameras are both in forward and backward scattering with respect to the incident or the reflected beam and the intensity differences between cameras are reduced. The calibration consists in a first guess realized with a 3D 2-level calibration plate, and is then refined by a volume self-calibration (**?**) until reaching a disparity lower than 0.2 pixel. The image processing consists in a subtraction of the time-average of the camera images. The volume reconstruction consists in 4 MART iterations (**?**) ; the ghost ratio is smaller than 10% and the normalized intensity variance larger than 35. The velocity

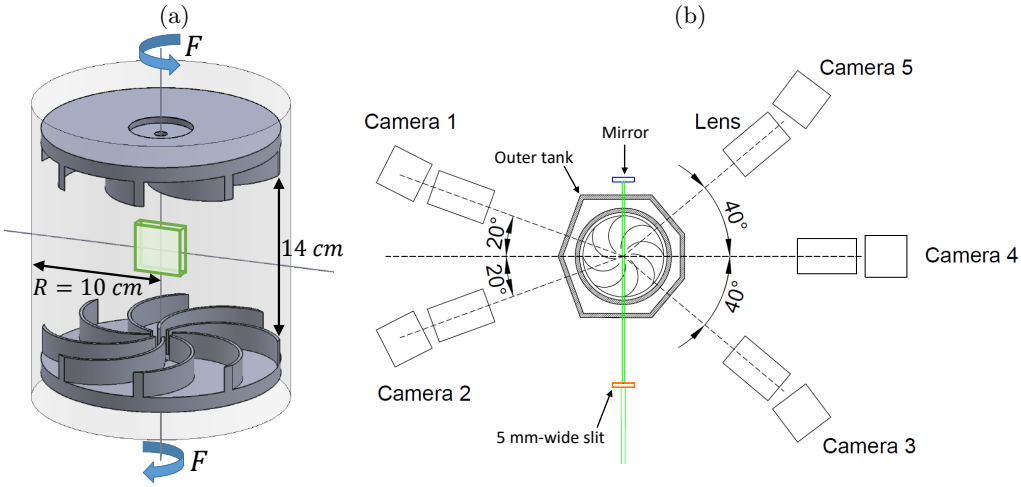

FIGURE 1. Experimental set-up. (a) Perspective view of the von Kármán flow geometry. The green area at the center is the measurement volume. (b) Top view of the whole set-up.

Case	T1	T2	T3	T4
F (Hz)	5	1	0.5	0.1
Reynolds number Re	3.1×10^5	6.3×10^4	3.1×10^4	6.3×10^3
Taylor Reynolds number R_λ	890	390	250	80
Kolmogorov length scale η (mm)	0.016	0.054	0.09	0.3
dx/η	22	6.5	3.8	1.2
Taylor length scale λ (mm)	0.96	2.1	2.8	5.3
Estimation of the number of independent velocity fields	4800	1600	1300	3800

TABLE 1. Parameters of the four different experimental cases.

fields are then obtained by a 4-step multi-pass volume correlation with window shifting and deformation ; Gaussian interrogation volumes are used, they overlap at 75%. The final interrogation volume size is 80 pixels, or 1.4 mm in the measurement volume. The space step is thus $dx = 0.35$ mm, and there are around $150 \times 100 \times 20$ velocity vectors. All the TPIV steps are performed with Davis software of LaVision company.

Varying the impeller rotation frequency F allows us to modify the Reynolds number of the flow Re, and thus the Kolmogorov scale $\eta = R(Re^3\epsilon^*)^{-1/4}$. With a constant TPIV resolution, we can thus probe different scale ranges, from the inertial range to the dissipative one : indeed, dx being constant, dx/η is increasing with Re. We considered four cases, whose characteristics are summarized in Tab. 1 : cases T1 and T2 allow us to probe the inertial range of scales, case T3 the transition range between the inertial and the dissipative ranges and case T4 allows us to probe the dissipative range. In this latter case, as the dissipative scales are resolved, it is possible to estimate the uncertainty on

the velocity based on the rms of the velocity divergence (**?**) ; we found an uncertainty of 0.3 pixel. In this work, we look for rare events ; thus, a large amount of uncorrelated velocity fields should be acquired. In our case, we accumulated in each case about 40 000 correlated frames, resulting in about 10 times less uncorrelated fields ; the last line of Tab. 1 gives an estimation of the number of independent velocity fields in each case, depending on the acquisition frequency.

PIV is a measurement method with a finite resolution : indeed, a velocity field measured by PIV can be seen as the real velocity field averaged over the interrogation volume. Therefore, PIV has a filtering effect, with a filter 3 dB-cut-off wavenumber well approximated by $k_{PIV} = 2.8/X$ where X is the interrogation volume size (**?**). Π^{ℓ}_{DR} can also be seen as a filtered quantity, whose filter is ϕ^{ℓ}. In this work, we use $\phi^{\ell}(\mathbf{x}) \propto e^{-30\mathbf{x}^2/(2\ell^2)}$. As a consequence, computing Π^{ℓ}_{DR} for velocity fields measured by PIV leads to a double filtering. It must then be ensured that the second filter (ϕ^{ℓ}) does not filter less than the first one (the PIV filter). This is ensured if the 3 dB-cut-off wavenumber of ϕ^{ℓ} is smaller than k_c, i.e. if $\sqrt{30\ln(2)}/\ell \leqslant k_{PIV}$. In the physical space, the corresponding relevant scales are $\ell_c = \pi\ell/\sqrt{30\ln(2)}$ and $\pi/k_{PIV} \approx X$: therefore, the double filtering is meaningful if $\ell_c \geqslant X$. In the following, we will mainly use ℓ_c as it can be directly compared to X ; it should always be understood as $\ell_c(\ell)$. According to the UV locality principle (**?**), computing Π^{ℓ}_{DR} on an already-filtered velocity field is meaningful as long as ℓ_c/X is large enough (and as long as the local Holder exponent is larger than 0) : indeed, the contribution to Π^{ℓ}_{DR} is mainly due to neighbouring scales ; therefore, too small scales can be ignored. In this paper, we present results obtained for $\ell_c = 1.7X$. Such size is a compromise between constraints inherent to TPIV and constraints to allow physical behaviors identification .

3. Statistics of Π^{ℓ}_{DR} with respect to scales and intensity of the extreme events

Our experimental set-up allows us to collect a large amount of velocity fields in order to have a statistically relevant sample and thus to observe very strong events. In this section, we report the behavior of the space-time average and of the probability distribution function (pdf) of Π^{ℓ}_{DR} before giving the intensity of the extreme events of Π^{ℓ}_{DR} studied in this article.

Fig. 2 shows the space-time average of Π^{ℓ}_{DR} and $\mathscr{D}^{\ell}_{\nu}$ at four values of ℓ_c/η, each one obtained with one of the cases T1 to T4. $\mathscr{D}^{\ell}_{\nu}$ is defined as follows :

$$\mathscr{D}^{\ell}_{\nu}(\mathbf{x}) = \nu \int \Delta\phi^{\ell}(\boldsymbol{\xi}) \frac{\delta\mathbf{u}^2}{2} d^3\boldsymbol{\xi} \tag{3.1}$$

It measures the viscous dissipation, and is used here rather than the usual $\nu\boldsymbol{\nabla}\mathbf{u}^{\ell} : \boldsymbol{\nabla}\mathbf{u}^{\ell}$ because it appears in the so-called weak Kármán-Howarth-Monin (**?**) along with Π^{ℓ}_{DR} .

Integrals involving the velocity increments can be seen as convolution products of the velocity field with a derivative of the filtering function (first derivative for Π^{ℓ}_{DR} , second derivative for $\mathscr{D}^{\ell}_{\nu}$). They are therefore first computed in the Fourier space as a scalar product of the Fourier transform of the velocity field and of the Fourier transform of the chosen derivative of the filtering function. The convolution product in the real space is then obtained by Fourier-transforming the scalar product obtained in the Fourier space. As experimental velocity fields are discrete and of finite dimensions, not all scales can be investigated but only scales between the space step and the interrogation volume size roughly. The lower and upper scales probed are discussed in more details in **?**.

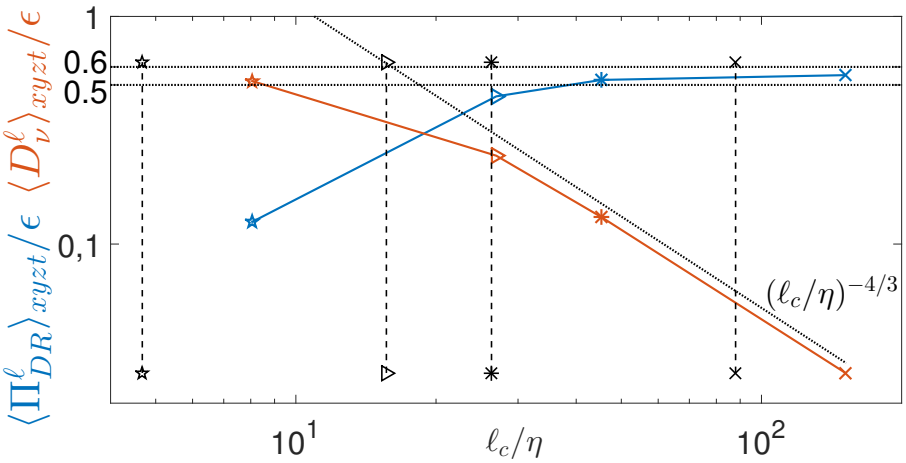

FIGURE 2. Space-time average of Π^ℓ_{DR} (blue) and $\mathscr{D}^\ell_\nu$ (red) with respect to scales. The vertical dashed lines correspond to the interrogation window size (divided by η). Pentagons : $\ell_c/\eta = 8$ (obtained with case T4), triangles : $\ell_c/\eta = 27$ (obtained with case T3), star : $\ell_c/\eta = 45$ (obtained with case T2), cross : $\ell_c/\eta = 150$ (obtained with case T1). The dotted line corresponds to the scaling $(\ell_c/\eta)^{-4/3}$.

It can be shown that the limit of $\mathscr{D}^\ell_\nu$ is the same as the limit of $\nu \boldsymbol{\nabla} \mathbf{u}^\ell : \boldsymbol{\nabla} \mathbf{u}^\ell$:

$$\lim_{\ell \to 0} \mathscr{D}^\ell_\nu = \nu \partial_j u_i \partial_j u_i$$

As expected, Π^ℓ_{DR} increases and $\mathscr{D}^\ell_\nu$ decreases with ℓ_c/η ; in the dissipative range, the viscous effects ($\mathscr{D}^\ell_\nu$) dominate the inertial effects (Π^ℓ_{DR}) whereas it is the contrary in the inertial range. In the inertial range, both Π^ℓ_{DR} and $\mathscr{D}^\ell_\nu$ seem to follow the Kolmogorov scalings : saturation of Π^ℓ_{DR} and decrease of $\mathscr{D}^\ell_\nu$ as $\ell^{-4/3}$. This average behavior supports the ability of our multi-scale analysis method to probe different scale ranges.

However, the pdfs in Fig. 3 show that Π^ℓ_{DR} and $\mathscr{D}^\ell_\nu$ do not have similar behaviors : whereas $\mathscr{D}^\ell_\nu$ has almost log-normal pdfs and scale-invariant centered-reduced pdfs, the pdfs of Π^ℓ_{DR} have wide tails ; also, the centered-reduced pdfs of Π^ℓ_{DR} are more skewed and have larger positive tails in the dissipative range. Note that the saturation of the pdfs of $\mathscr{D}^\ell_\nu$ at low values are most probably spurious and due to the computation of this term. Whereas $\mathscr{D}^\ell_\nu$ takes only positive values, Π^ℓ_{DR} also has negative values, but its pdfs are skewed towards positive values, and this skewness is stronger in the dissipative range.

Tab. 3 gives the values of the 10th and 1000th largest events of $|\Pi^\ell_{DR}|$ at different values of ℓ_c/η, in terms of ϵ and of σ, the standard deviation of the distribution of Π^ℓ_{DR} . In Sec. 4, the structure of the velocity field at the 1000 strongest events of $|\Pi^\ell_{DR}|$ is analyzed with the VGT method and in Sec. 5, the structure of the velocity field around the 10 strongest events only is analyzed by direct observation. Even if Π^ℓ_{DR} takes smaller values in average in the dissipative range, it can still reach very large values, almost equal to 100ϵ, i.e. 200 times the average $\mathscr{D}^\ell_\nu$ at the same scale, or 270 the standard deviation of the pdf of Π^ℓ_{DR}. Interpreting Π^ℓ_{DR} as an energy inter-scale transfer rate towards smaller scales, this strongly suggests that there is not a unique dissipative scale, which would be the smallest flow scale, as smaller scales are necessary to dissipate such large transfer at this value of ℓ_c. This is in agreement with the phenomenological interpretation of the multifractal model (**?**), which suggests that there is a finite range of dissipative scales, which depend on the local smoothness of the velocity field. In the inertial range, the

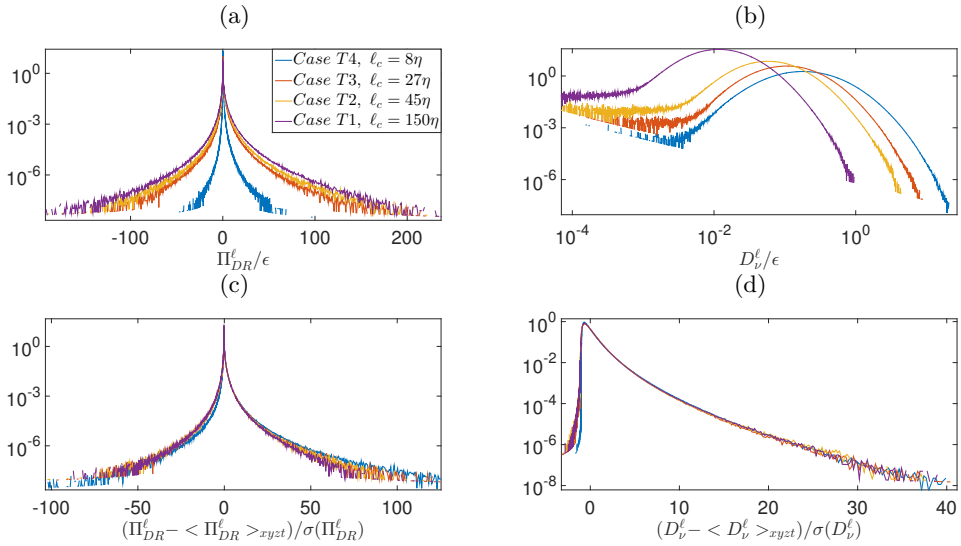

FIGURE 3. Probability density functions of Π^ℓ_{DR} and of the viscous dissipation $\mathscr{D}^\ell_\nu$ for cases T1 to T4. The vertical axes are in logarithmic coordinates and the horizontal axes in linear coordinates except for (b) where it is in logarithmic coordinates. Blue : $\ell_c/\eta = 8$ (case T4) ; red : $\ell_c/\eta = 27$ (case T3) ; orange : $\ell_c/\eta = 45$ (case T2) ; purple : $\ell_c/\eta = 150$ (case T1). (a) Pdf of Π^ℓ_{DR} normalized by the global dissipation rate ϵ (computed from torque measurements). (b) Pdf of $\mathscr{D}^\ell_\nu$ normalized by the global dissipation rate ϵ. (c) Centered-reduced pdf of Π^ℓ_{DR}. (d) Centered-reduced pdf of $\mathscr{D}^\ell_\nu$.

ℓ_c/η	8	27	45	150
Largest $\lvert\Pi^\ell_{DR}\rvert$	97ϵ	360ϵ	320ϵ	330ϵ
	270σ	210σ	150σ	120σ
10th largest $\lvert\Pi^\ell_{DR}\rvert$	58ϵ	190ϵ	190ϵ	250ϵ
	160σ	110σ	90σ	90σ
1000th largest $\lvert\Pi^\ell_{DR}\rvert$	14ϵ	48ϵ	56ϵ	73ϵ
	38σ	29σ	27σ	27σ

TABLE 2. Values of the 10th and 1000th largest events of $|\Pi^\ell_{DR}|$ at different values of ℓ_c/η. "$x\epsilon$" means that the value is equal to x times the global average dissipation rate measured by torquemeters, "$x\sigma$" means that the value is equal to the space-time average of Π^ℓ_{DR} plus x times the (space-time) standard-deviation of Π^ℓ_{DR} .

extremes of Π^ℓ_{DR} take larger values in terms of ϵ than in the dissipative range, but these extremes are smaller in terms of standard deviations. This is in agreement with the behavior of the raw and centered-reduced pdfs.

4. Characterization using the VGT invariants

We first characterize the extreme events of Π^ℓ_{DR} by computing the invariants of the VGT which capture the local topology of the flow. The average behavior of Π^ℓ_{DR} and $\mathscr{D}^\ell_\nu$ with respect to the topology can thus be studied, and the distribution of the topology in the whole flow and among the extreme events of Π^ℓ_{DR} can be compared.

According to **?**, the local topology of a 3D regular-enough velocity field can be characterized by the invariants of the VGT $\boldsymbol{\nabla}\mathbf{u}$ at the studied point. Let us call $Q = -tr((\boldsymbol{\nabla}\mathbf{u})^2)/2$ the second invariant, and $R = -tr((\boldsymbol{\nabla}\mathbf{u})^3)/3 = -det(\boldsymbol{\nabla}\mathbf{u})$ the third invariant of the VGT. For a 3D incompressible flow, the first VGT invariant which is $tr(\boldsymbol{\nabla}\mathbf{u})$ is zero everywhere as the flow is divergence-free ; therefore, the sum of the VGT eigenvalues is 0 and there are only four possible configurations or topologies, based on the two following criteria : (i) either there are only real eigenvalues (for $27R^2+4Q^3<0$), or one real and two complex-conjugate eigenvalues ($27R^2+4Q^3>0$) and (ii) either two eigenvalues have a positive real part (for $R>0$) or only one eigenvalue has a positive real part ($R<0$), the remaining eigenvalue(s) having a negative real part. The four topologies are :

- the "filament" (F), when $27R^2+4Q^3<0$ and $R<0$. The fluid is compressed in two directions and stretched in the third one.
- the "sheet" (S), when $27R^2+4Q^3<0$ but $R>0$. The fluid is compressed in one direction and stretched in the two others.
- the "vortex stretching" (VS), or stable focus/stretching, when $27R^2+4Q^3>0$ and $R<0$. In one plane, the motion of the fluid is a converging spiral ; in the remaining direction the fluid is stretched.
- the "vortex compressing" (VC), or unstable focus/compressing, when $27R^2+4Q^3>0$ but $R>0$. The fluid is compressed in one direction ; in the plane containing the two other directions, its motion is a diverging spiral.

In this work, we compute the VGT on an experimental velocity field which is smoothed at the resolution scale by the measurement method. Therefore, the velocity field is regular and applying the VGT invariant method is meaningful. The obtained topology is the topology of the flow "at the resolution scale".

The distribution of the four topologies in the flow can be easily obtained by computing the VGT and its invariants everywhere and forming the joint pdf of Q and R. This joint pdf was observed to have a tear-drop shape for different types of flow, in both experimental and numerical works (**??**). We also find this particular shape when the dissipative scales are resolved, as shown in Fig. 4(a). When the dissipative scales are not resolved, the joint pdf is closer to a square, as can be seen in Fig. 4(b). The percentage of each topology can be obtained by integrating the pdf over each domain, they are given in the second column of tables Tab. 3 and Tab. 4. Vortex stretching and compressing are the most probable topologies, but they are less probable in the dissipative range, for the benefit of the sheet topology.

The global distribution of topologies can now be compared with the distribution of topologies among the 1000 strongest events of $|\Pi^\ell_{DR}|$ in order to check whether a particular topology is favored by the extreme events of $|\Pi^\ell_{DR}|$, which may come along non-viscous dissipation. The percentage of each topology among the 1000 strongest events of $|\Pi^\ell_{DR}|$ is given in the third column of tables Tab. 3 and Tab. 4 for $\ell_c/\eta=8$ and $\ell_c/\eta=150$ respectively. At $\ell_c/\eta=150$, extreme events of $|\Pi^\ell_{DR}|$ cannot be associated with possible non-viscous dissipation because ℓ_c is too large, but we give their value to compare the behavior of Π^ℓ_{DR} in the dissipative and inertial ranges. The vortex stretching topology is clearly favored among extreme events of $|\Pi^\ell_{DR}|$. This is especially pronounced in the

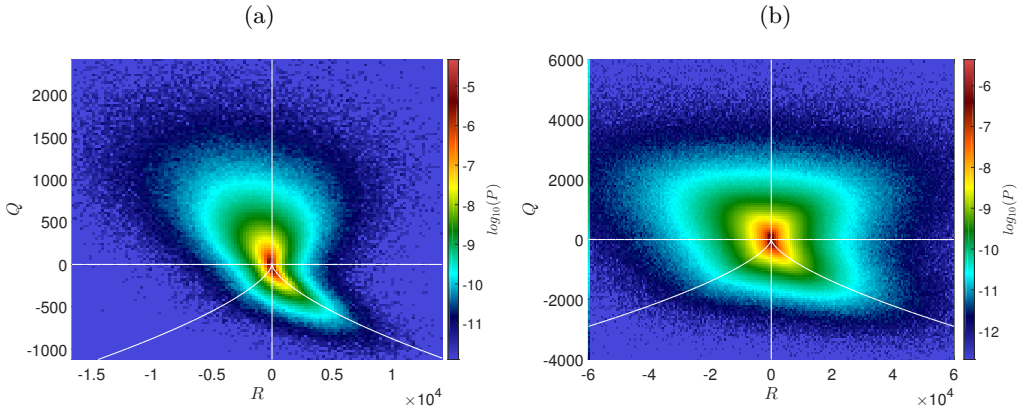

FIGURE 4. Joint pdfs of the second and third invariants of the VGT Q and R. (a) $\ell_c/\eta = 8$ (case T4). (b) $\ell_c/\eta = 150$ (case T1). White lines : $Q = 0$, $R = 0$ and $27R^2 + 4Q^3 = 0$ (Vieillefosse line).

Topology	Whole flow	1000 first extreme events of	
		Π^ℓ_{DR}	$\mathscr{D}^\ell_\nu$
Vortex stretching	37%	60%	68%
Vortex compressing	31%	21%	27%
Sheet	22%	13%	4%
Filament	10%	6%	2%

TABLE 3. Distribution of the topologies obtained with the VGT method for $\ell_c/\eta = 8$ (case T4).

dissipative range. We also give the distribution of topologies among the 1000 strongest events of $\mathscr{D}^\ell_\nu$. Extreme events of $\mathscr{D}^\ell_\nu$ seem to favor the vortex stretching topology too, even more than extreme events of $|\Pi^\ell_{DR}|$. The real-eigenvalued topologies are much less probable than among the 1000 strongest events of $|\Pi^\ell_{DR}|$.

Extreme events of $|\Pi^\ell_{DR}|$ and $\mathscr{D}^\ell_\nu$ favor the vortex stretching at the expense of the other topologies. One can therefore wonder whether these terms depend on the topology, i.e. on Q and R. This can be investigated by studying the conditional averages of Π^ℓ_{DR} and $\mathscr{D}^\ell_\nu$ conditioned on Q and R. They are plotted in Fig. 5 for $\ell_c/\eta = 8$ and $\ell_c/\eta = 150$. Though they are scattered on the sides (large $|Q|$ and $|R|$), which is expected as such events are rare and do not allow for convergence of the conditional average, clear trends can be observed for smaller values of $|Q|$ and $|R|$. The largest values of $|\Pi^\ell_{DR}|$ seem to be obtained in the sheet topology area both in the dissipative ($\ell_c/\eta = 8$) and inertial ranges ($\ell_c/\eta = 150$). This is quite at variance with the distribution of extremes conditioned on the 1000 strongest events of $|\Pi^\ell_{DR}|$. However, a zone of large $|\Pi^\ell_{DR}|$ can be observed in the vortex stretching zone, at large negative values of R, for Q around or slightly less than 0 (with smaller values than in the sheet zone though). This zone corresponds to

Topology	Whole flow	1000 first extreme events of	
		Π^ℓ_{DR}	$\mathscr{D}^\ell_\nu$
Vortex stretching	40%	44%	51%
Vortex compressing	36%	37%	39%
Sheet	14%	11%	6%
Filament	10%	8%	4%

TABLE 4. Distribution of the topologies obtained with the VGT method for $\ell_c/\eta = 150$ (case T1).

small values of Q, meaning that the enstrophy is dominated by the strain. The extreme events of $|\Pi^\ell_{DR}|$ corresponding to vortex stretching probably come from this area. The conditional average of Π^ℓ_{DR} is not the same in the dissipative and in the inertial range. In particular, the zone of negative Π^ℓ_{DR} is in the vortex compressing area in the dissipative range, whereas it is in the vortex stretching area in the inertial range. This shows that the value of Π^ℓ_{DR} does not depend only on the topology (i.e. Q and R). The conditional average of $\mathscr{D}^\ell_\nu$ is more consistent with the distribution of the four topologies among the 1000 strongest events of $\mathscr{D}^\ell_\nu$: the conditional average of $\mathscr{D}^\ell_\nu$ takes large values in the vortex stretching zone, both for very large values of Q and in the area where large values of the conditional average of Π^ℓ_{DR} were observed, and in the vortex compressing zone. The isolines of the conditional average of $\mathscr{D}^\ell_\nu$ resemble the isolines of the QR joint pdf.

The analysis of the VGT invariants showed that the extreme events of $|\Pi^\ell_{DR}|$ mainly correspond to a zone of the vortex stretching area where the strain dominates the enstrophy. Such an analysis gives only information at the point where the extreme value is found, but ignores the structure velocity field around it. In the next section, we describe the structures of the velocity field observed around these extreme points.

5. Characterization by direct observation of the velocity fields

In order to characterize the velocity field on a larger area around the extreme events of $|\Pi^\ell_{DR}|$, we observed :

- the velocity streamlines,
- the Π^ℓ_{DR} and $\mathscr{D}^\ell_\nu$ fields,
- and the isosurfaces of the vorticity

for the ten strongest $|\Pi^\ell_{DR}|$ events and for each case.

For case T4, i.e. when the dissipative scales are resolved by our measurement method, we observed three kinds of structures : the “screw-vortex”, the “roll-vortex”, and the “U-turn”. The screw-vortex is characterized by streamlines that spiral in a single direction, whereas the roll-vortex is characterized by streamlines that roll-up and then spiral in two opposite directions. An example of a screw-vortex is shown in Fig. 6 and an example of a roll-vortex is shown in Fig. 7. The U-turn is characterized by a sharp bend of the streamlines ; an example is shown in Fig. 8. For all structures, Π^ℓ_{DR} takes large

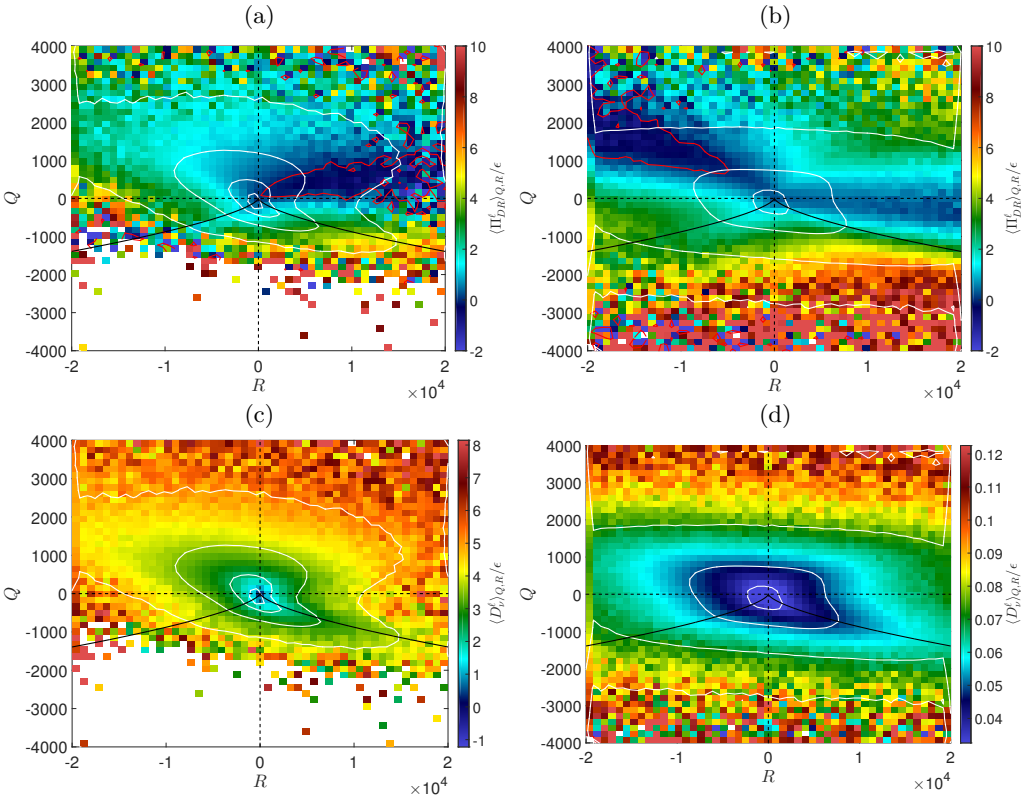

FIGURE 5. Conditional average of Π^ℓ_{DR} and $\mathscr{D}^\ell_\nu$ conditioned on the VGT second and third invariants Q and R. The white lines correspond to isovalues of the QR joint pdf. The red lines correspond to $\langle \Pi^\ell_{DR}\rangle_{Q,R} = 0$. The black plain line corresponds to the Vieillefosse line $27R^2 + 4Q^3 = 0$. (a) Conditional average of Π^ℓ_{DR} for $\ell_c/\eta = 8$ (case T4). (b) Conditional average of Π^ℓ_{DR} for $\ell_c/\eta = 150$ (case T1). (c) Conditional average of $\mathscr{D}^\ell_\nu$ for $\ell_c/\eta = 8$ (case T4). (b) Conditional average of $\mathscr{D}^\ell_\nu$ for $\ell_c/\eta = 150$ (case T1).

positive and negative values along the structure, but in the case of U-turns, the largest $|\Pi^\ell_{DR}|$ corresponds to a negative Π^ℓ_{DR} whereas for the vortices it corresponds either to a positive or negative Π^ℓ_{DR}. All structures display large values of the velocity (three times the rms of the fluctuations). This is in accordance with the predicted divergence of the velocity norm in the case of a singularity occuring in a solution to the 3D INSE (**?**), which would be the source of inertial dissipation. The observed structures also display large values of the vorticity (of the order of the maximum vorticity observed in all the velocity fields, i.e. 20 to 30 times the standard deviation of the vorticity) and of $\mathscr{D}^\ell_\nu$ (of the order of the maximum $\mathscr{D}^\ell_\nu$ observed in all the velocity fields, i.e. 30 times the standard deviation of $\mathscr{D}^\ell_\nu$). Actually, some of the ten strongest events of $|\Pi^\ell_{DR}|$ are also among the 10 strongest events of vorticity or of $\mathscr{D}^\ell_\nu$. In the case of the screw- and roll-vortices, the isosurfaces of the vorticity are tubes ; in the case of U-turns, they are either tubes or pancakes. $\mathscr{D}^\ell_\nu$ takes large values around but outside the zones of large vorticity ; zones of large $\mathscr{D}^\ell_\nu$ are also shifted compared to zones of large $|\Pi^\ell_{DR}|$, they seem to better follow the symmetry of the structures compared to zones of large $|\Pi^\ell_{DR}|$.

For cases T1 to T3, i.e. when only the inertial scales are resolved by our measurement technique, similar structures were found except that they were more distorted or more complex : globally, it is possible to recognize one of the three structures mentioned above

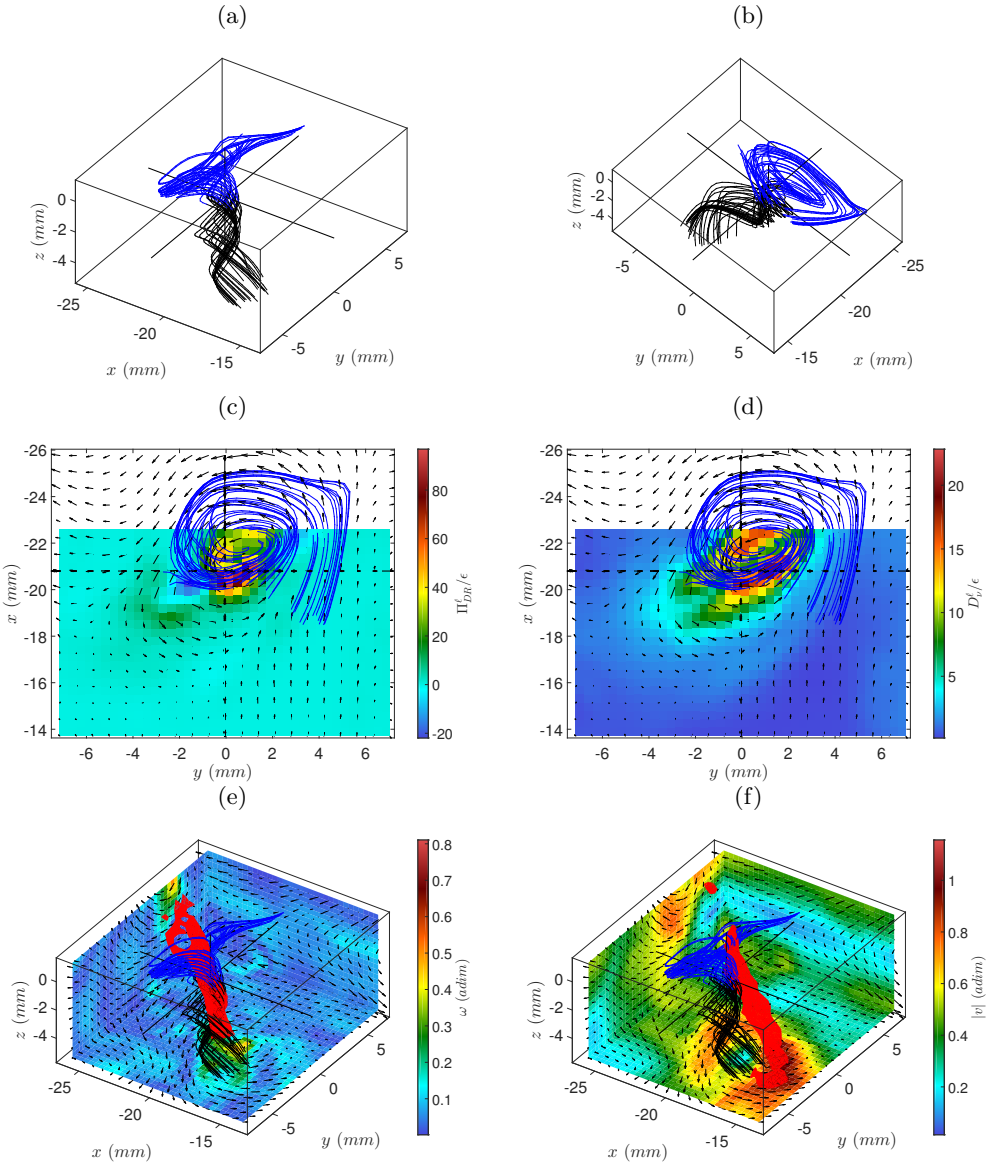

FIGURE 6. Velocity field around the 1st extreme event of Π^{ℓ}_{DR} of case T4. (a) Velocity streamlines. (b) Velocity streamlines from another point of view. (c) In-plane velocity field (arrows) and Π^{ℓ}_{DR} field (color) in the (xy) plane containing the extreme event. (d) In-plane velocity field (arrows) and $\mathscr{D}^{\ell}_{\nu}$ field (color) in the (xy) plane containing the extreme event. (e) In-plane velocity field (arrows) in three (xy), (xz) and (yz) planes bounding the observed area, vorticity norm (color on these planes), velocity streamlines and isosurface of the vorticity norm (isolevel : 0.41). (f) In-plane velocity field (arrows) in three (xy), (xz) and (yz) planes bounding the observed area, velocity norm (color on these planes), velocity streamlines and isosurface of the velocity norm (isolevel : 0.92). Blue streamlines are arriving around the extreme event of Π^{ℓ}_{DR} whereas black ones are leaving the extreme zone.

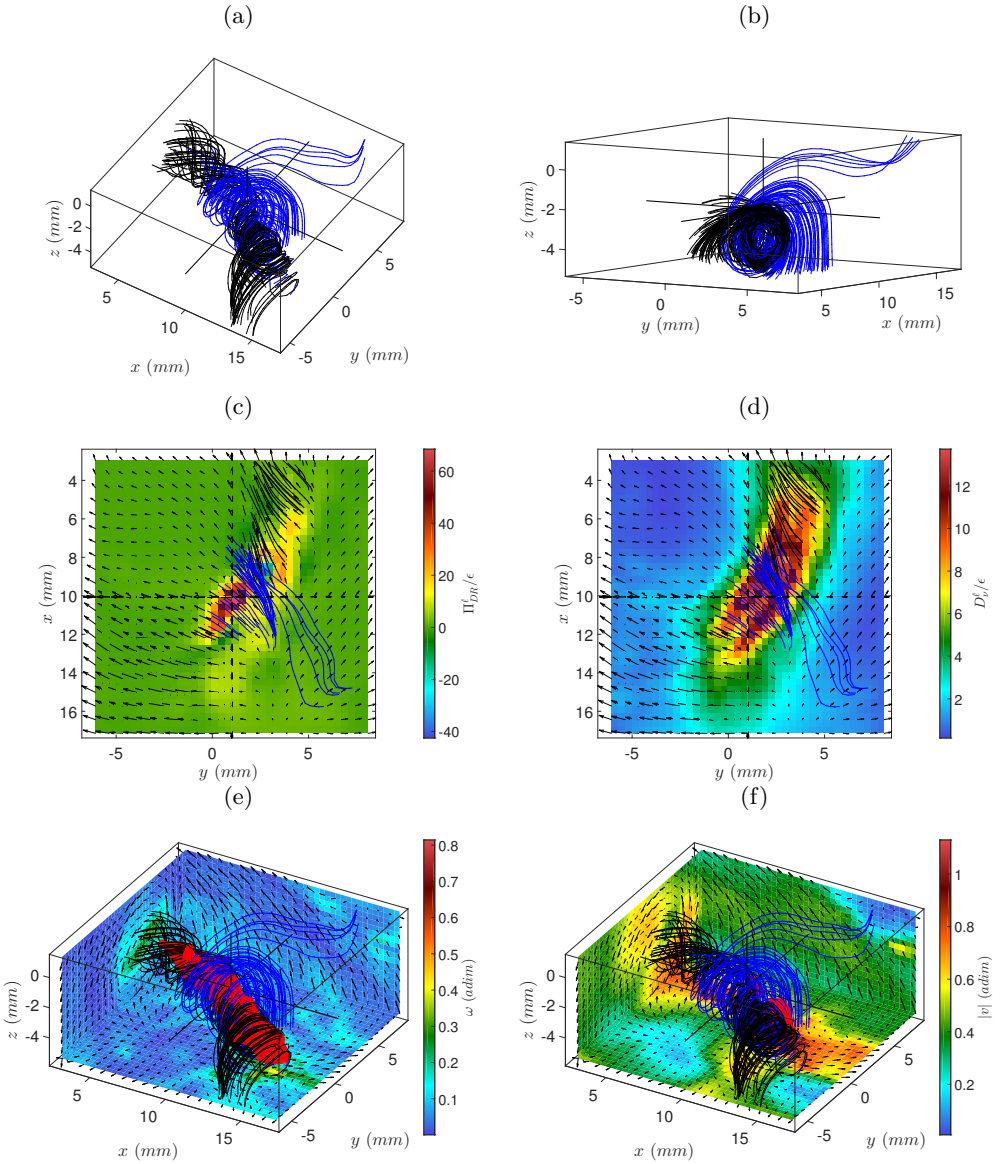

FIGURE 7. Velocity field around the 5th extreme event of Π^{ℓ}_{DR} of case T4. (a) Velocity streamlines. (b) Velocity streamlines from another point of view. (c) In-plane velocity field (arrows) and Π^{ℓ}_{DR} field (color) in the (xy) plane containing the extreme event. (d) In-plane velocity field (arrows) and $\mathscr{D}^{\ell}_{\nu}$ field (color) in the (xy) plane containing the extreme event. (e) In-plane velocity field (arrows) in three (xy), (xz) and (yz) planes bounding the observed area, vorticity norm (color on these planes), velocity streamlines and isosurface of the vorticity norm (isolevel : 0.33). (f) In-plane velocity field (arrows) in three (xy), (xz) and (yz) planes bounding the observed area, velocity norm (color on these planes), velocity streamlines and isosurface of the velocity norm (isolevel : 0.77). Blue streamlines are arriving at zones of large vorticity whereas black ones are leaving such zones.

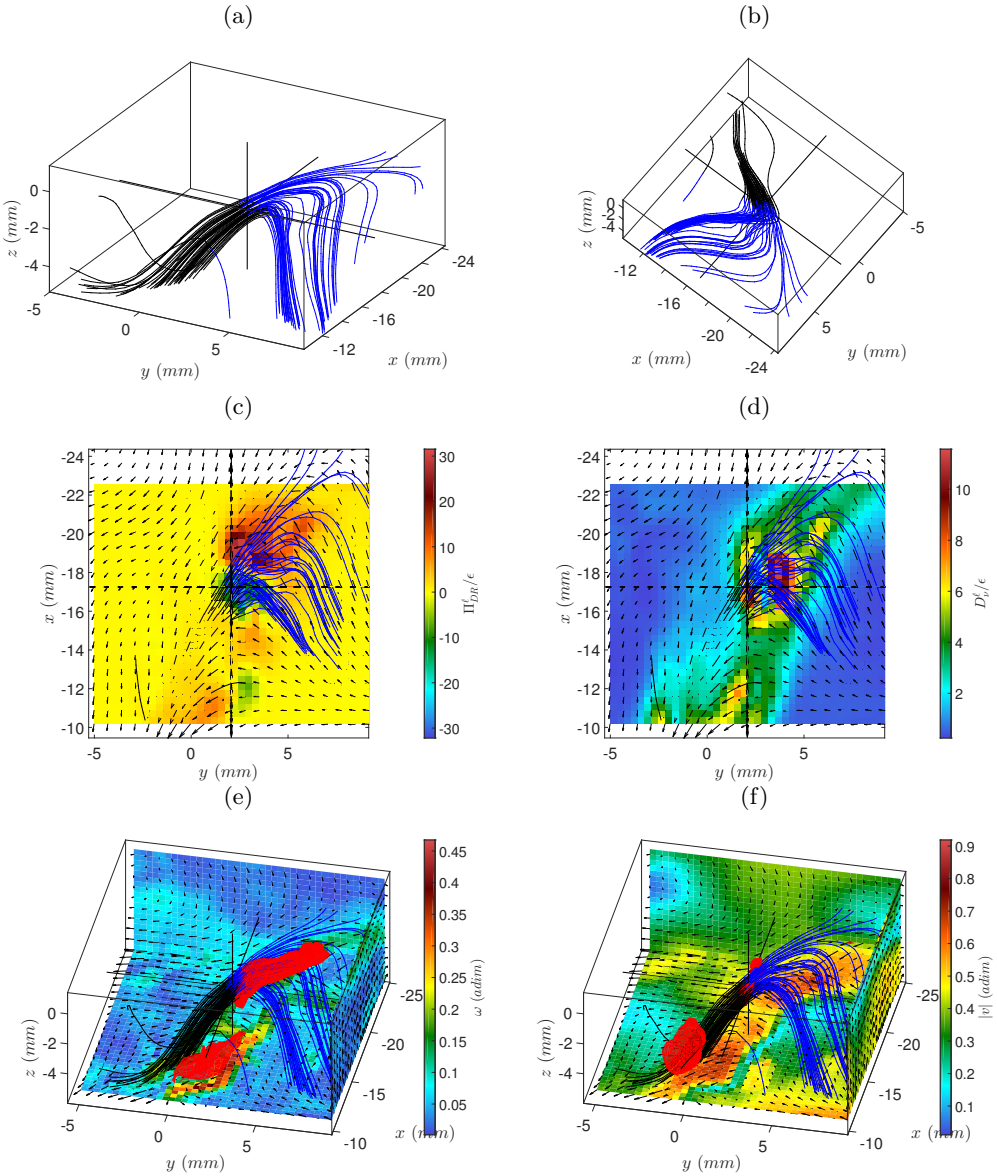

FIGURE 8. Velocity field around the 5th negative extreme event of Π^{ℓ}_{DR} of case T4. (a) Velocity streamlines. (b) Velocity streamlines from another point of view. (c) In-plane velocity field (arrows) and Π^{ℓ}_{DR} field (color) in the (xy) plane containing the extreme event. (d) In-plane velocity field (arrows) and $\mathscr{D}^{\ell}_{\nu}$ field (color) in the (xy) plane containing the extreme event. (e) In-plane velocity field (arrows) in three (xy), (xz) and (yz) planes bounding the observed area, vorticity norm (color on these planes), velocity streamlines and isosurface of the vorticity norm (isolevel : 0.33). (f) In-plane velocity field (arrows) in three (xy), (xz) and (yz) planes bounding the observed area, velocity norm (color on these planes), velocity streamlines and isosurface of the velocity norm (isolevel : 0.77). Blue streamlines are arriving around the extreme event of Π^{ℓ}_{DR} whereas black ones are leaving the extreme zone.

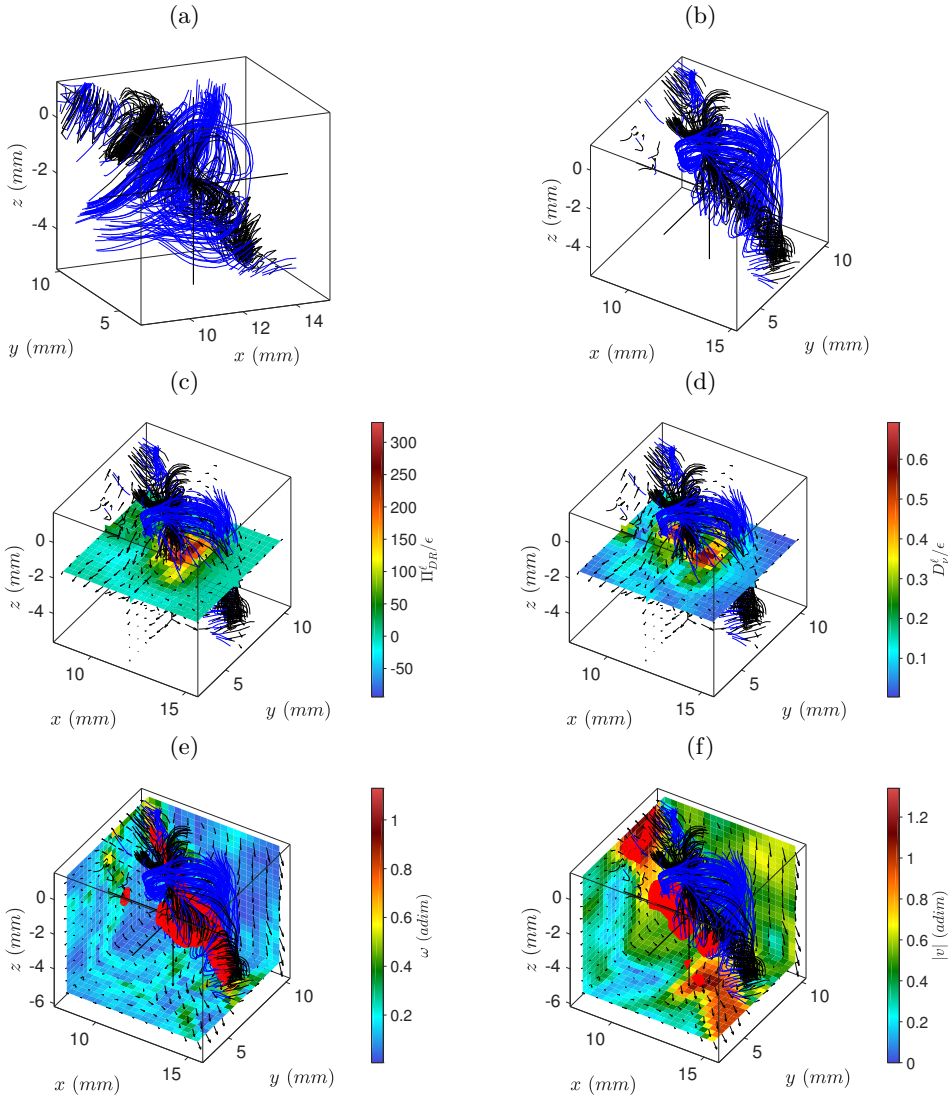

FIGURE 9. Velocity field around the 1st extreme event of Π^{ℓ}_{DR} of case T1. (a) Velocity streamlines. (b) Velocity streamlines from another point of view. (c) In-plane velocity field (arrows) and Π^{ℓ}_{DR} field (color) in the (xy) plane containing the extreme event. (d) In-plane velocity field (arrows) and $\mathscr{D}^{\ell}_{\nu}$ field (color) in the (xy) plane containing the extreme event. (e) In-plane velocity field (arrows) in three (xy), (xz) and (yz) planes bounding the observed area, vorticity norm (color on these planes), velocity streamlines and isosurface of the vorticity norm (isolevel : 0.68). (f) In-plane velocity field (arrows) in three (xy), (xz) and (yz) planes bounding the observed area, velocity norm (color on these planes), velocity streamlines and isosurface of the velocity norm (isolevel : 1.13). Blue streamlines are arriving around the zones of large Π^{ℓ}_{DR} whereas black ones are leaving such zones.

but fluctuations at smaller scales could be observed. This is consistent with the fact that the resolution is larger than the dissipative scales for these cases, and therefore that there exists fluctuations over scales smaller than the resolution. An example of roll-vortex is shown in figure Fig. 9 : it is possible to distinguish the streamlines that roll-up and then

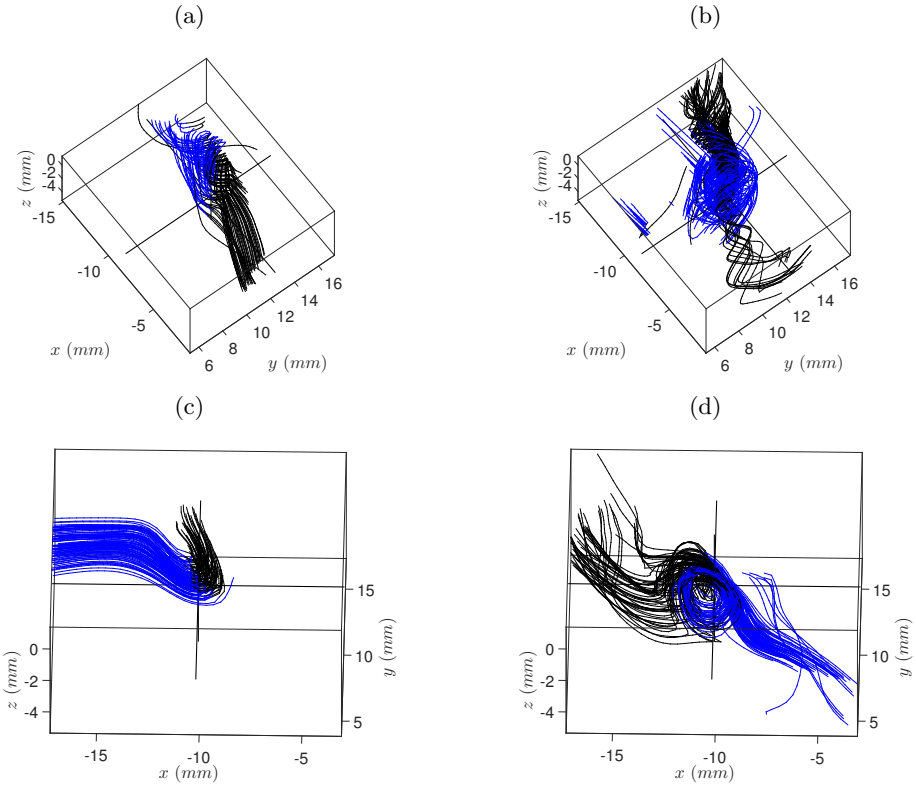

FIGURE 10. Impact of the frame of reference on the velocity field aspect. (a) Velocity streamlines around the 2nd extreme event of Π^{ℓ}_{DR} of case T4 seen in the laboratory frame of reference. (b) Velocity streamlines around the same event but in the frame of reference having a constant velocity (equal to the spatial average of the velocity over the observed field) with respect to the laboratory frame. (c) Velocity streamlines around the 2nd negative extreme event of Π^{ℓ}_{DR} of case T4 seen in the laboratory frame of reference. (d) Velocity streamlines around the same event but in the frame of reference having a constant velocity (equal to the velocity at the extreme point) with respect to the laboratory frame. Blue streamlines are arriving towards zones of high vorticity whereas black ones are leaving such zones. The three black lines intersect at the point where Π^{ℓ}_{DR} is maximum.

spiral in two opposite directions, but the structure is twisted and less smooth than in the roll-vortex in Fig. 7.

6. Discussion

Three different kinds of structures seem to emerge from the analysis of the velocity fields around the extreme events of $|\Pi^{\ell}_{DR}|$. However, in some cases, they may represent the same event, seen in different frames of reference or at different times. For instance, a roll-vortex which is advected at a velocity oriented along its axis will look like a screw-vortex in the laboratory frame of reference, as shown in Fig. 10 (a) and (b). On the contrary, if it is advected at a velocity oriented perpendicularly to its axis, it will look like a U-turn in the laboratory frame, as shown in Fig. 10 (c) and (d). On the other hand, it is sometimes difficult to find the inertial frame in which a given structure would look like a roll-vortex, and when the vorticity isosurfaces are pancake-like, in the case of some U-turn, it is impossible to find such an inertial frame : indeed, the vorticity is the same in

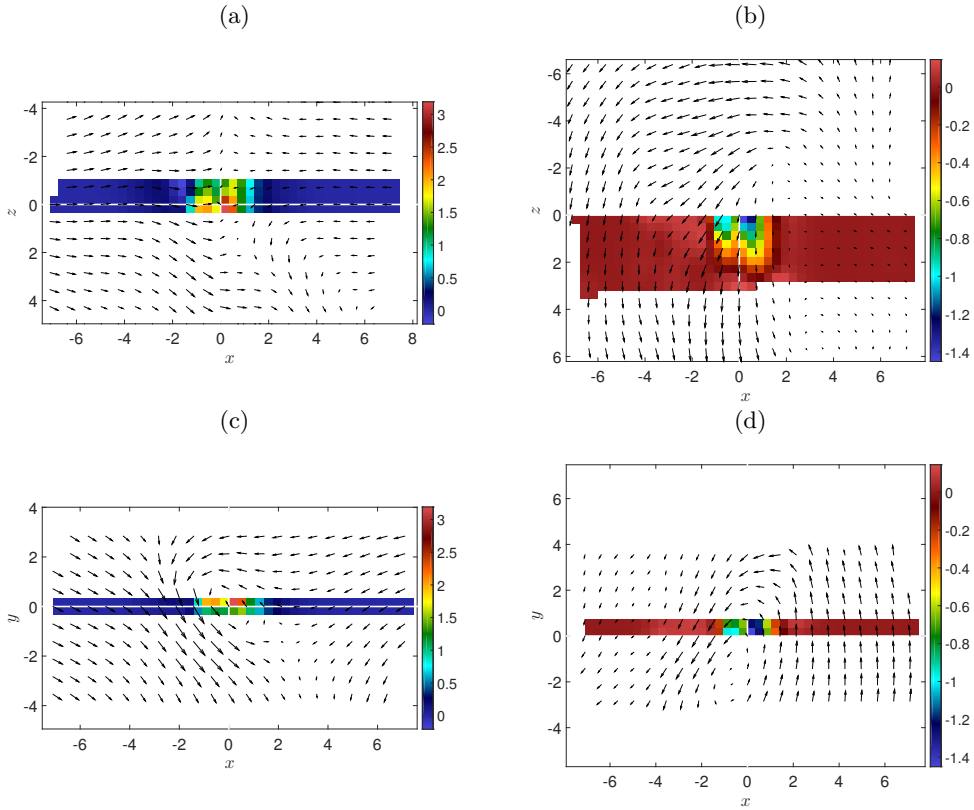

FIGURE 11. Examples of the 2D structures reported in **?**and observed in our results. The arrows correspond to the in-plane velocity field and the color to the dimensionless term Π^{ℓ}_{DR}. (a) Front : top view of the 6th extreme event of Π^{ℓ}_{DR} of case T4. (a) Jet : top view of the 8th negative extreme event of Π^{ℓ}_{DR} of case T4. (c) Spiral : front view of the 6th extreme event of Π^{ℓ}_{DR} of case T4. (d) Cusp : front view of the 8th negative extreme event of Π^{ℓ}_{DR} of case T4.

any inertial frame, so it is not possible to find one where its isosurfaces would be tubes, as is expected from a roll-vortex. However, it is possible that the three different structures correspond to a single one, seen at different times. For instance, in **?**, the authors observe a roll-up of vorticity sheets, giving vorticity tubes. This suggests that the U-turn with pancake-like vorticity isosurfaces would appear first, and would evolve towards a U-turn with tube-like vorticity isosurfaces, then followed by a vortex, whose vorticity isosurface is tube-like. Time-resolved measurements will allow for confirmation of this mechanism. Screw-vortices may also be remainings of roll-vortices after a possible split. Constructing formula for the observed topologies is not that easy because of limited spatial resolution in the z direction; in a parallel unpublished numerical study of these events (Nguyen et al 2020), we have however noticed that these structures bear some similarities with the asymmetric Burgers stretched vortices, studied in **?**.

Our results compare well with results in **?**, where the structure of 2D velocity fields around events of a 2D version of Π^{ℓ}_{DR} is studied. Four 2D structures where observed : spirals, cusps, fronts and jets. We could identify these four 2D structures in particular cross-sections of our three 3D structures. For instance, let us consider the 6th extreme event of Π^{ℓ}_{DR} of case T4, which is a roll-vortex : a cross-section perpendicular to the vortex axis reveals a spiral (Fig. 11(c)) whereas a cross-section containing the vortex

axis gives a front (Fig. 11(a). Indeed, a roll-vortex occurs when two bodies of fluid meet each other ; one of them then rolls up and spirals in two directions. In a plane containing the axis, the spiral cannot be seen, contrary to the splitting in two directions : this is a front. Let us now consider the 8th negative extreme event of Π^{ℓ}_{DR} of case T4, which is a U-turn with a strong shear : looking at it from the front gives a cusp (Fig. 11(d)) whereas looking at it from the top reveals a jet (Fig. 11(b)).

Our results also compare well with numerical works at similar Reynolds numbers : **?** (90^3 grid, $R_\lambda = 90$) and **?** (240^3 grid, $R_\lambda = 240$). Indeed, extreme events of $|\Pi^{\ell}_{DR}|$ come along with very large values of the vorticity, so that we can compare them with the large vorticity structures studied in those works. Note that it is not sure whether zones of large vorticity always come along with large values of $|\Pi^{\ell}_{DR}|$: it seems that large $|\Pi^{\ell}_{DR}|$ leads to large vorticity norms, but the contrary remains to prove. Both kinds of events may correspond to prints of singularities (see introduction and **?**), and the difference between them, if so, could shed some light on the problem. In accordance with those works, we observed that vorticity isosurfaces were either tubes or pancakes and that zones of large dissipation were surrounding the zones of large vorticity. This is at variance with more recent simulations with a larger Reynolds number (**?**) (8192^3 grid, $R_\lambda \approx 1300$). In this work, stronger vorticity events are observed, with vorticity isosurfaces being blob-like and zones of large dissipation being colocated with zones of large vorticity. This colocation of the large vorticity and large dissipation zones is also observed in the stationary singular solutions of **?**. The discrepancy between our experimental result and these numerical results may however be a spurious effect since it is known that they are very sensitive to the spatial and temporal resolution (**?**). In particular, the resolution of $\Delta x = 1.5\eta$ used in the large Reynolds number simulation may not be sufficient, so that small scale structure may not be properly resolved. Indeed, intermittency of the dissipations calls for over-resolved simulations, for instance down to one tenth of the Kolmogorov scale **?**. Note that this problem does not occur in our experiment because even if the resolution measurement is around the Kolmogorov scale, smaller (unobserved) scales can nevertheless develop and impact the larger scales.

The fact that many of our events are associated with vortex compression might be a symptom of a link with vortex reconnection, as one might expect vortex compression immediately following such reconnection. We are currently preforming time-resolved measurements to confirm this point. Note that yet unpublished numerical work (Nguyen et al, 2020) indeed support such conjecture.

7. Conclusion

In this paper we studied the structure of the turbulent velocity fields around extreme events of Π^{ℓ}_{DR} computed in the dissipative range. Such events may be precursors to non-viscous dissipation. We performed our analysis on 3D velocity fields measured by TPIV at the center of a von Kármán flow ; at the smaller turbulent Reynolds number, our resolution is of the order of the Kolmogorov scale. The strongest $|\Pi^{\ell}_{DR}|$ events we detected in the dissipative range reach 100 times the global average dissipation rate. We used two approaches to characterize the structure of the velocity field around these events : we studied the velocity gradient tensor invariants at the extremes and we observed the velocity fields and derived quantities. The conditional average of Π^{ℓ}_{DR} conditioned on the VGT second and third invariants seems to be the largest in the sheet zone, but the most extreme events of $|\Pi^{\ell}_{DR}|$ mostly correspond to the vortex stretching topology. The direct observation of the velocity fields allowed for identification of three different structures : the screw- and roll- vortices, and the U-turn. They may correspond to a

single structure seen at different times or in different frames of reference. The extreme events of $|\Pi^{\ell}_{DR}|$ come along with large velocity and vorticity norms, and the structure of the vorticity field around these events agrees with previous observations of numerical works at similar Reynolds numbers. It is at variance with more recent observations at larger Reynolds numbers though. The agreement of our results with numerical results is encouraging and validates our experimental approach ; time-resolved measurements are in progress to investigate the link between the three observed structures. Also, the relation between Π^{ℓ}_{DR} and the vorticity should be clarified, in order to check whether the detection criteria based on these two scalars are equivalent or whether the occurence of both a large $|\Pi^{\ell}_{DR}|$ and a large vorticity leads to special structures. An important headway regarding the problem of singularities would be made by checking whether the observed structures persist at even smaller scales or not. This will be achieved in a future work by improving the experimental resolution, together with investigations at larger Reynolds numbers as the occurence of singularities may be conditioned on this parameter.

Declaration of Interests. The authors report no conflict of interest.

Acknowledgements We thank anonymous referees for helpful comments, and Maurice Rossi for discussions about the structure of the velocity field around the extreme events. This work has been funded by the ANR, project EXPLOIT, grant agreement no. ANR-16-CE06-0006-01, and project ECOUTURB grant agreement no. ANR-16-CE30-0016.